Nano Research Energy

ISSN 2791-0091 (print); 2790-8119 (online)
https://doi.org/10.26599/NRE.2025.9120157

Research Article

A cost-effective multifunctional molecule for efficient and stable invert perovskite solar cells

Yaoyao Li[1,2], Jiaqun Li[3], Ning Meng[1,2], Haoze Han[3], Jianfeng Yan[3] (✉), and Dandan Song[1,2] (✉)

[1] *Key Laboratory of Luminescence and Optical Information, Beijing Jiaotong University, Ministry of Education, Beijing 100044, China*
[2] *Institute of Optoelectronics Technology, Beijing Jiaotong University, Beijing 100044, China*
[3] *State Key Laboratory of Tribology in Advanced Equipment, Department of Mechanical Engineering, Tsinghua University, Beijing 100084, China*

Received: 29 December 2024 / **Revised:** 17 February 2025 / **Accepted:** 24 February 2025 / **Published date:** 3 April 2025

ABSTRACT

Interlayer modification between the perovskite and charge transport layers is critical to minimize trap-assisted recombination losses and promote highly efficient and stable perovskite solar cells. However, the cost and complexity of most modification materials limit the rapid development of perovskite photovoltaic technology. In this study, we propose Tris(1-chloro-2-propyl) phosphate (TCPP) as a cost-effective and efficient solution for interfacial modification. Theoretical calculations and experimental results demonstrate that the P=O group in TCPP effectively passivate both deep energy level defects and shallow defects of perovskite. This interaction enhances crystallinity, leading to high-quality films and improved solar cell efficiencies, achieving up to 20.73%. Our work presents the potential of organic molecules constructed with P=O group for enhancing both the efficiency and stability of perovskite solar cells, paving the way for their commercial viability.

KEYWORDS

perovskite, solar cell, surface passivation, multifunctional molecule

1 Introduction

Over the past decade, organic-inorganic metal hybrid perovskites have emerged as potential substitutes to traditional photovoltaic materials, owing to their compelling innate properties, which include high absorption coefficient [1], tunability of band gap [2], extended exciton diffusion length [3], elevated carrier mobilities [4], and low exciton binding energy [5]. Although the power conversion efficiency (PCE) of perovskite solar cells (PSCs) exceeds 26% [6], several challenges hinder their commercial viability. A primary concern is defect formation at interfaces and within the bulk perovskite material [7, 8], which promotes increased charge carrier recombination and reduced carrier lifetime [9]. Additionally, these defects expedite PSC degradation due to susceptibility to moisture and ion migration [10, 11]. Consequently, optimizing perovskite crystallization and passivating perovskite films to mitigate defects are crucial for achieving high PCE and long-term environmental stability in PSCs [12, 13]. Besides, ultrafast laser processing enables the precise fabrication of specific micro/nanostructures on devices, which can effectively modulate their optical properties and substantially enhance their photovoltaic performance [14, 15].

Recent studies have identified two main causes that have limited the efficiency of inverted PSCs: the degree of crystallization within the perovskite itself and the interfacial nonradiative recombination losses [16–19]. Innovative interface materials and additives designed to overcome these limitations. These materials work through various mechanisms, such as binding with uncoordinated Pb^{2+} ions to reduce defects and creating insulating layers to minimize surface recombination and boost open circuit voltage (V_{OC}) [20–23]. Ideal interface materials and additives should meet several criteria: they must form a compact, well-defined structure that thoroughly covers the perovskite layer, exhibit resilience against environmental and operational stressors, align energetically with the perovskite layer for efficient charge transfer, and possess the ability to passivate defects effectively. A well-engineered interlayer not only shields the perovskite from water and oxygen infiltration but also stabilizes the cell against the release of volatile components, ensuring the long-term durability of PSCs [24–26].

Despite extensive research reporting various interface materials that enhance the performance of perovskite devices and exploring their passivation effects, the precise mechanisms by which these materials achieve passivation and the specific types of defects they target still require further investigation. Furthermore, the impact of top-interface materials on the crystallization quality of perovskite films remains unclear. It is generally assumed that interface materials do not affect the intrinsic film quality of perovskites but instead modify the interfacial properties [27, 28].

Address correspondence to Jianfeng Yan, yanjianfeng@tsinghua.edu.cn; Dandan Song, ddsong@bjtu.edu.cn

The Lewis acid-base theory provides a robust framework for understanding defect passivation in perovskites. Undercoordinated Pb^{2+} ions at surfaces and grain boundaries act as Lewis acid sites due to their electron-deficient nature, while functional groups with lone electron pairs (e.g., P=O, C=O, -NH_2) serve as Lewis bases. The strength of this interaction depends on the electron-donating capacity of the Lewis base and the electron-accepting ability of the Lewis acid. In perovskite systems, effective passivation requires Lewis bases with moderate to high basicity. Strong Lewis bases form stable coordination bonds with Pb^{2+}, neutralizing defect states and suppressing non-radiative recombination. Conversely, weak Lewis bases exhibit limited passivation efficacy due to insufficient electron donation. Phosphorus-oxygen (P=O) bonds are particularly effective in this context. The high electronegativity of phosphorus (2.19 Pauling scale) and the polarized nature of the P=O bond (dipole moment ~3.5 D) endow these groups with exceptional Lewis basicity. This enables P=O to act as a potent electron donor, forming stable coordination complexes with Lewis acidic Pb^{2+} ions (electronegativity: 2.33) at perovskite surfaces. Tris(1-chloro-2-propyl) phosphate (TCPP), widely used as a halogenated flame retardant, emerges as a promising candidate due to its affordability, excellent thermal conductivity, hydrolytic stability, and insolubility in water and aliphatic hydrocarbons. Its unique composition, featuring phosphorus-oxygen functional groups and chlorine elements, is conducive to the growth and optimization of perovskite films [29].

In this work, we explore the top interface modification method to improve the quality of perovskite films and performance of PSCs. TCPP was applied onto the perovskite layer through an in-situ reaction. This novel approach led to the development of PSCs with efficiencies reaching from 18.83% up to 20.73%, representing a notable improvement in achieving high-performance and stable PSCs. Additionally, we conducted density functional theory (DFT) calculations to elucidate the mechanism by which TCPP passivates defects in the perovskite structure.

2 Results and discussion

Figure 1(a) shows the chemical structure of TCPP, which includes organophosphorus ligands, chlorine (Cl) elements, oxygen (O) elements, and a carbon chain skeleton. The organophosphorus ligands are used for interfacial modification in interface engineering, allowing them to bind to the surface of perovskite films and passivate defects through coordination bonds between the electron-rich O element in the organophosphorus ligand and the undercoordinated Pb^{2+} in the perovskite. To reveal the interaction between TCPP and perovskite, DFT calculation is conducted as shown in Fig. 1(b), which shows that TCPP can effectively bind to a Pb-rich perovskite surface through interactions with Pb atoms. Moreover, we calculate the passivation effects of TCPP on different defects in perovskite solar cells demonstrating its versatile passivation capability across multiple defect types. Defects in perovskite solar cells can be categorized into two main types: deep energy level defects, exemplified by Pb cluster defects (Fig. S1(c) in the Electronic Supplementary Material (ESM)), and shallow energy level defects, such as I vacancy defects (Fig. S1(d) in the ESM) [30–32]. Therefore, we further investigate the effect of TCPP on Pb cluster defects, demonstrating the bonding between the Pb cluster and P=O groups, as depicted in Fig. 1(c). The density of states (DOS) comparison before and after TCPP modification as well as ideal perovskite (without any defect) are presented in Fig. 1(e). TCPP's multidentate coordination capability enables simultaneous passivation of multiple defect types. For Pb cluster defects (Fig. 1(c)), the P=O···Pb interaction eliminates deep trap states, as evidenced by the DOS comparison in Fig. 1(e). The DOS profile of TCPP-treated perovskite closely resembles that of ideal perovskite, indicating effective deep-level defect passivation. Following TCPP treatment, the DOS in deep states is effectively eliminated, approaching that of ideal perovskite, demonstrating TCPP's passivation capability in deep defect passivation. Additionally, we assessed the influence of P=O on I vacancy defects. For I vacancy defects (Fig. 1(d)), the interaction between P=O and the defect site repairs shallow states near the conduction band minimum (CBM). The DOS comparison in Fig. 1(f) shows that TCPP treatment suppresses shallow trap states, enhancing charge extraction efficiency. It was observed that P=O groups are absorbed on the perovskite surface when TCPP is used to address these defects, as shown in Fig. 1(d), I vacancy defects introduce localized shallow state defects at the CBM of the perovskite [33]. Figure 1(f) illustrates the DOS of perovskite with I vacancy defects, ideal perovskite, and perovskite after TCPP passivation. Notably, the interaction between P=O and I vacancy causes significant changes in the band-edge state, leading to the repair of shallow defects via electrostatic interaction. For I vacancy defects (Fig. 1(d)), the interaction between P=O and the defect site repairs shallow states near the CBM. The DOS comparison in Fig. 1(f) shows that TCPP treatment suppresses shallow trap states, enhancing charge extraction efficiency. In conclusion, TCPP effectively passivates both deep and shallow defects through coordination passivation.

PSCs were fabricated based on the structure with ITO/PTAA/perovskite/TCPP/PCBM/BCP/Ag, as illustrated in Fig. 2(a). The optimal TCPP concentration was determined to be 0.25 wt.%, as evidenced by the results shown in Figs. 2(b) and 2(c). Based on this result, all subsequent experiments were conducted using this optimized concentration. The *J*–*V* characterizations of the additive-modified devices are shown in Fig. 2(c), and the details are given in Table S1 in the ESM. The PCE of the control device is 18.83%, with an V_{OC} of 1.15 V, a short circuit density (J_{SC}) of 22.73 mA·cm^{-2}, and a fill factor (FF) of 72.11%, the champion PCE of the TCPP modified devices reach 20.73%, accompanied by a V_{OC} of 1.16 V, a J_{SC} of 23.89 mA·cm^{-2}, and an FF of 74.88%. To verify the reliability and operational stability of these devices, we monitored their steady-state output PCE at the maximum power point (MPP), as shown in Fig. 2(e). This enhancement in PCE can be attributed to the effective defect passivation by TCPP, which reduces non-radiative recombination losses and improves charge transport efficiency. Figure 2(f) depicts the impact of the TCPP passivation on the external quantum efficiency (EQE) and integrated J_{SC} of the PSCs. It is obvious that the PSCs with TCPP-passivated perovskite films exhibit higher EQE in the entire measurement range in comparison to the non-passivated device. This indicates a decrease carriers' recombination in TCPP-passivated PSCs, which is consistent with the calculation results as shown in Fig. 1.

To investigate the underlying reasons for the performance enhancement, X-ray diffraction (XRD) was utilized to investigate the crystalline structure of the perovskite films, as illustrated in Fig. 3(a). Based on the diffraction peaks, it is evident that the material exhibits a perovskite phase. The characteristic peaks at approximately 20.2°, 32.0°, and 40.8° corresponding to the cubic phase of the perovskite. These peaks remain unchanged after TCPP modification. Notably, the relative intensity of certain peaks

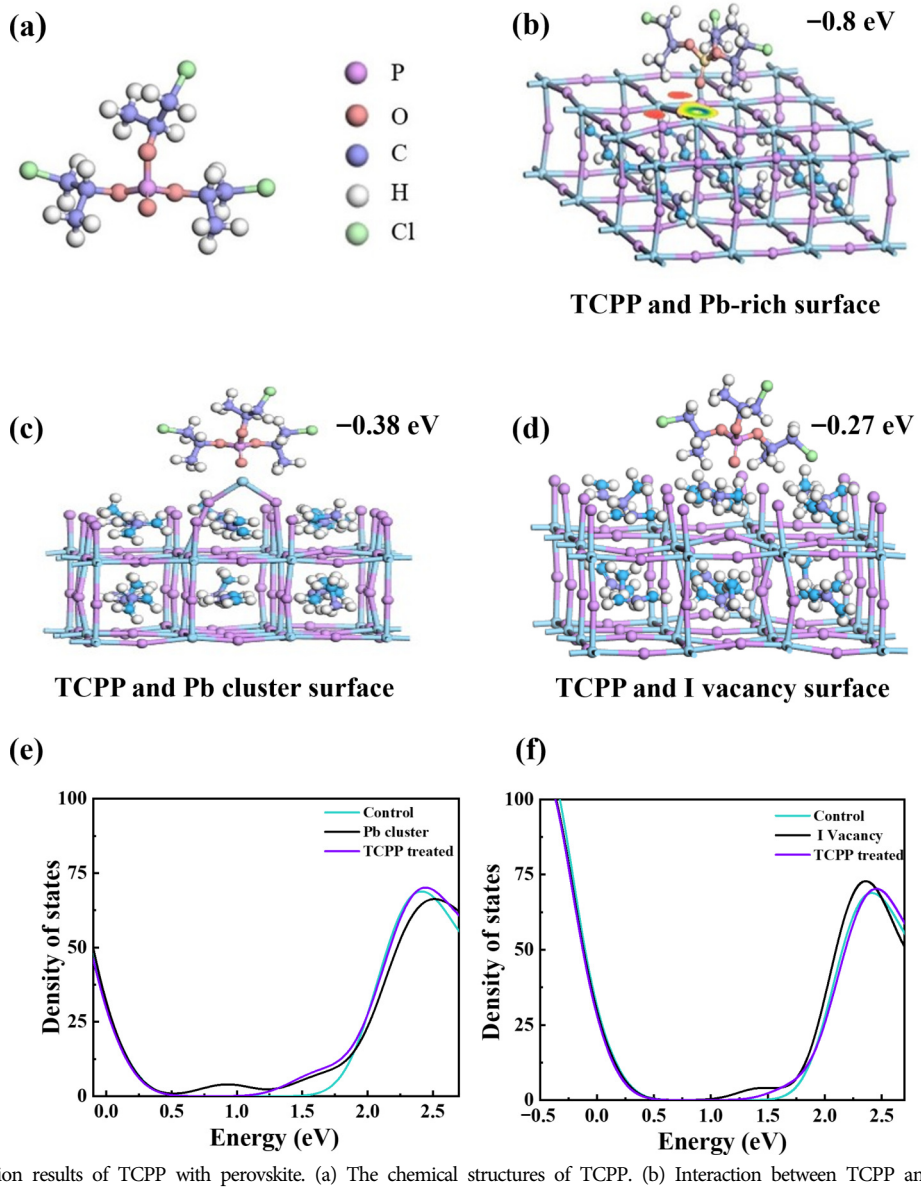

Figure 1 DFT calculation results of TCPP with perovskite. (a) The chemical structures of TCPP. (b) Interaction between TCPP and perovskite from DFT calculations. (c) and (e) Comparison of DOS of Pb-cluster defects on the FAI-terminated surface and the corresponding TCPP-passivated. (d) and (f) Comparison of DOS of I vacancy defects on the FAI-terminated surface and the corresponding TCPP-passivated.

changes after TCPP treatment, suggesting a reorientation of the perovskite crystals. This reorientation is attributed to the strong interaction between the P=O groups in TCPP and undercoordinated Pb^{2+} ions on the perovskite surface. The P=O groups act as Lewis bases, preferentially aligning with Pb^{2+} (Lewis acids) and stabilizing specific crystallographic planes during film formation. Furthermore, the diffraction peaks of the TCPP-modified film exhibit slightly higher intensity, indicating improved crystallinity. This enhancement is consistent with the observed reduction in trap states and improved device performance. However, the peak intensity at 12.6° of the crystallized PbI_2 shows a significant decrease after TCPP modification, indicating a substantial interaction between PbI_2 and TCPP. The strong interaction between TCPP and Pb effectively mitigates the surface residual Pb [34], which has been identified as a primary origin of deep-level trap states in perovskite films, which is in good agreement with DFT calculations. Using the ITO/perovskite structure, the effects of interface modification on the optoelectronic properties and charge carrier recombination kinetics of perovskite films are studied through steady-state photoluminescence (PL) and time-resolved photoluminescence (TRPL) decay measurements. Figure 3(b) demonstrates a more intense emission at 766 nm in TCPP-modified perovskite films, pointing to reduced charge quenching and nonradiative recombination compared to the control film. Moreover, TRPL decay analysis (Fig. 3(c)) revealed a fast component (τ_1) and a slow component (τ_2). The carrier lifetime of the perovskite films (see Fig. 3(e) and summarized in Table S2 in the ESM) was found to be extended by TCPP treatment (τ_1 = 63.43 ns, τ_2 = 226.34 ns , and the average lifetime (τ_{ave}) = 115.85 ns) compared to the control film (τ_1 = 52.50 ns, τ_2 = 181.48 ns, and τ_{ave} = 85.36 ns), further supporting the notion that TCPP is more effective in suppressing nonradiative carrier recombination and reducing trap states, further supporting the notion that TCPP is more effective in suppressing nonradiative carrier recombination and reducing trap states [35, 36]. This evidence demonstrates that during the post-treatment process, TCPP not only influences the defects within the interface but also the bulk of the perovskite, which

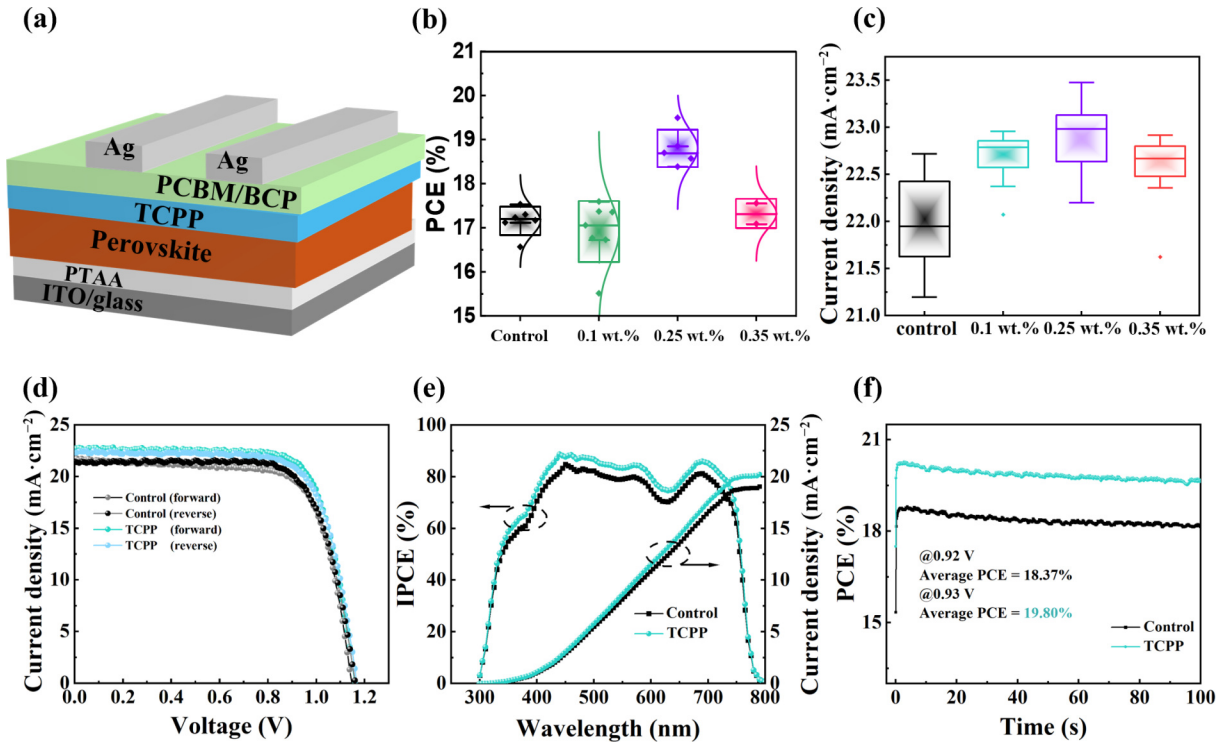

Figure 2 (a) Device structure of p-i-n planar PSCs. (b, c) The distribution of J_{SC} and PCE for different concentrations of TCPP modification. (d) *J*-*V* curves under forward and reverse scan. (e) IPCE spectra and integrated J_{SC} values of the PSCs. (f) The change of the PCE values in 100 s.

aligns with the observed continued growth of perovskite grains after TCPP treatment, The TCPP treatment effectively suppresses nonradiative carrier recombination and diminishes trap states on the surface of the perovskite film, thereby enhancing the potential for achieving high J_{SC} and PCE of the PSC [37]. Furthermore, the absorption properties of the perovskite film exhibit minimal change with TCPP, as demonstrated in Fig. 3(e), indicating that the enhanced J_{SC} is not caused by increased light absorption. Additionally, the optical bandgap of the perovskite films remains consistent at 1.62 eV, as calculated from the Tauc plot (Fig. 3(f)) [38]. These results indicate that TCPP modification primarily functions through defect passivation at surface and bulk states rather than altering the intrinsic optical properties of the perovskite film.

To further investigate the impact of TCPP post-treatment on the morphology of perovskite films, scanning electron microscopy (SEM) images of perovskite films with and without TCPP modification are shown in Figs. 4(a) and 4(b). Evidently, the average grain size of the modified film increases, indicating a reduction in grain boundaries within the organophosphorus ligand-modified membranes. Additionally, the TCPP-modified film diminishes numerous small holes on the control film, resulting in a smoother surface. Surface morphology of perovskite films was examined before and after TCPP post-treatment using atomic force microscopy (AFM), as depicted in Figs. 4(c) and 4(d). The post-treatment with TCPP decreased the root-mean-square (RMS) surface roughness from 16.4 nm in the original perovskite film to 13.9 nm. This reduction in surface roughness suggests that the modifier effectively covers the concave positions at the grain boundary [39], consistent with SEM observations. The morphological changes demonstrate that modification at the top interface of perovskite films can also promote secondary growth of the perovskite, affecting the overall film quality rather than merely altering the surface interface properties [40].

The surface energy is effectively modified by TCPP treatment. As shown in Figs. 5(a) and 5(b), the contact angle of the perovskite film is increased from 55.286° to 67.376° through TCPP treatment, enhancing the perovskite films' humidity resistance. We conducted an analysis of the surface composition and chemical interactions of perovskite films using X-ray photoelectron spectroscopy (XPS) (Fig. S2 in the ESM). In Fig. 5(c), the high-resolution spectra of the Pb_{4f} core level show peaks at approximately ~138 and ~143 eV, corresponding to $4f_{7/2}$ and $4f_{5/2}$, respectively [41, 42]. Upon the introduction of organophosphorus ligands, the peaks of $4f_{7/2}$ and $4f_{5/2}$ notably shift to lower binding energy compared to the control film with 0.2 eV, indicating coordination between the organophosphorus ligand and undercoordinated Pb^{2+} ion, leading to an increase in the electron density of the Pb atomic nucleus. This observation aligns with DFT calculations, which show the electron transfer from the electron-rich P=O group to the perovskite. In comparison to the standard device, the device modified with TCPP exhibited a lower Urbach energy (E_u), decreasing from 49 to 45 meV, suggesting a notable reduction in the defect density and structural disorder of the respective perovskite film [43], as depicted in Fig. 5(d). This reduction in Urbach energy indicates improved electronic quality of the perovskite film with sharper band edges and fewer sub-bandgap states [44, 45].

Figure 6(a) further carried out EIS analysis of PSCs, and the Nyquist plot showed that the spectra are coupled in the high frequency region into an impedance semicircle representing carrier transport between ETL/Perovskite/HTL interfaces [46, 47]. When the smaller the impedance value, the more favorable the carrier transport. The surface of PSC modified with TCPP showed significantly reduced charge transport resistance (R_{ct}), which is consistent with the results measured by PL and TRPL. Enhanced carrier extraction and/or improved carrier transport in the perovskite films, as well as low R_{ct} indicate that electrons are

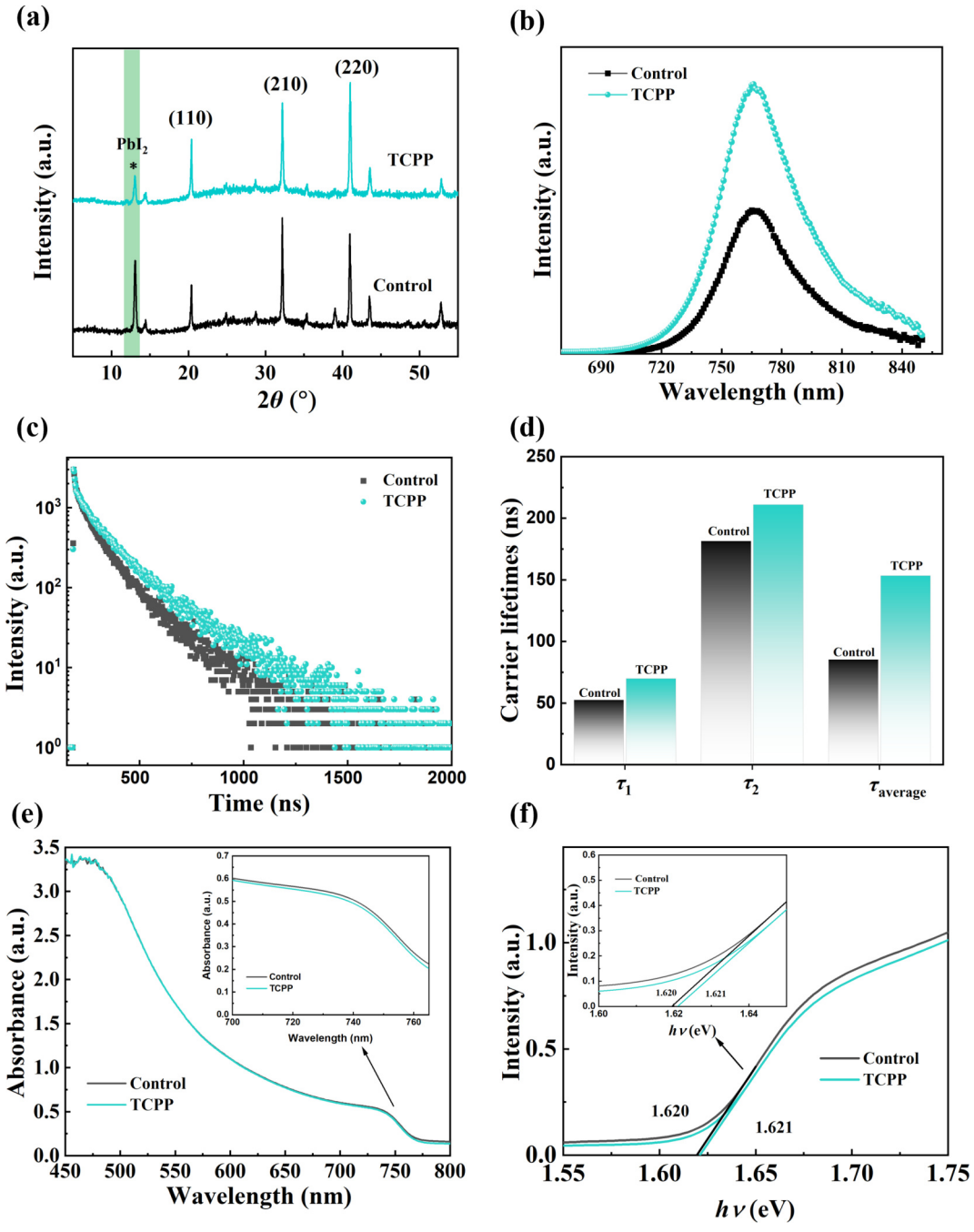

Figure 3 Characteristics of the control and modified perovskite films (a) XRD patterns. (b) Steady-state PL spectra. (c) and (d) TRPL spectra and their fitting parameters. (e) and (f) UV–vis absorption spectra and its Tauc plot.

moving rapidly in the solar cells, manifested as enhancement of J_{SC} in the device. Moreover, Mott-Schottky analysis was performed on the devices with and without interface material modifications. As illustrated in Fig. 6(b), the values of the built-in potential (V_{bi}) were extracted from the intercept at the *X*-axis (refer to Table S3 in the ESM for details). The TCPP-modified device exhibits a higher V_{bi} of 0.86 V compared to the control device (0.83 V), favoring carrier separation, transport, and extraction [48]. To delve deeper into the charge recombination mechanisms in the PSCs, we present the plots of V_{OC} on light intensity (P) in Fig. S3 in the ESM. Based on the slope of the dependence of V_{OC} versus P, we assess the extent of trap-assisted recombination using the equation: $V_{OC} = (nKT/q)\ln(P)$, where n represents the ideality factor, and K and T are the Boltzmann constant and absolute temperature, respectively. In comparison to the control device's value of 1.31 KT/q, the slope decreases to 1.14 KT/q for the TCPP-modified device, indicating effective suppression of defect-assisted recombination due to reduced defect density. Additionally, the plots of J_{SC} at different light intensities are illustrated in Fig. S4 in the ESM, where all types of PSCs exhibit a linear relationship with each slope close to unity, suggesting that bimolecular recombination in both PSCs is negligible. To delve deeper into the underlying mechanisms driving the varied properties of PSCs modified by control interface materials, we extracted the device parameters from the *J*–*V* curve depicted in Fig. 2(d). The device parameters of the PSC, such as the ideality factor of the diode (m), the series resistance (R_S), and the reverse saturation current (J_0) of the PSC, can be computed using the approach outlined in the

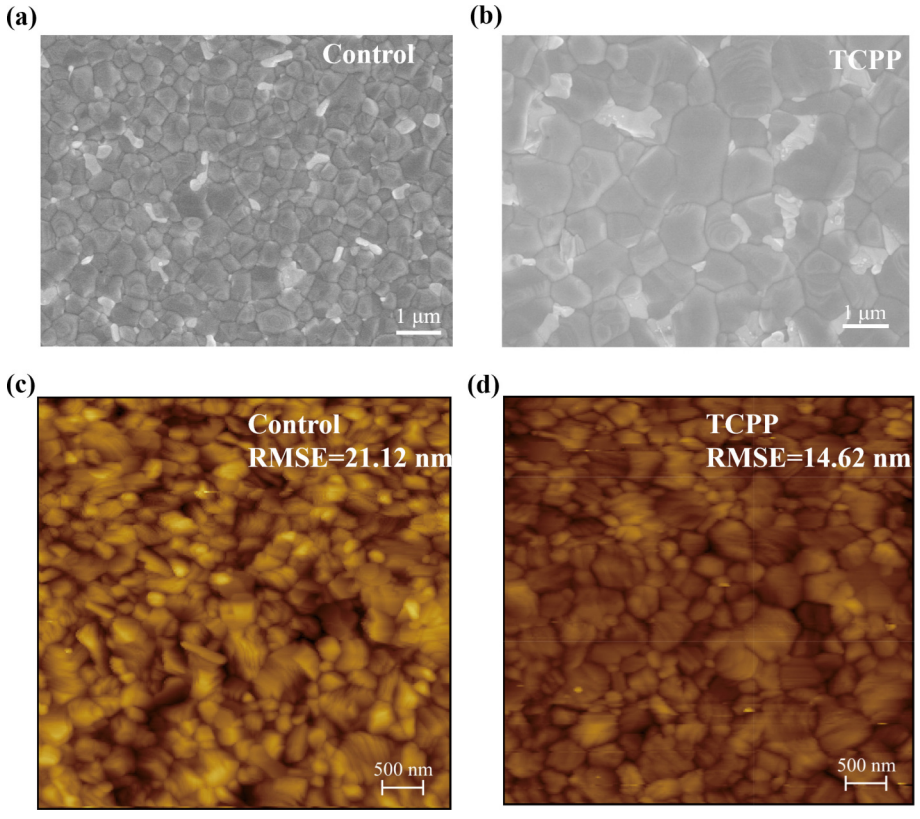

Figure 4 Surface characteristics of the control and modified perovskite films. (a) and (b) The top-view of SEM images. (c) and (d) AFM images.

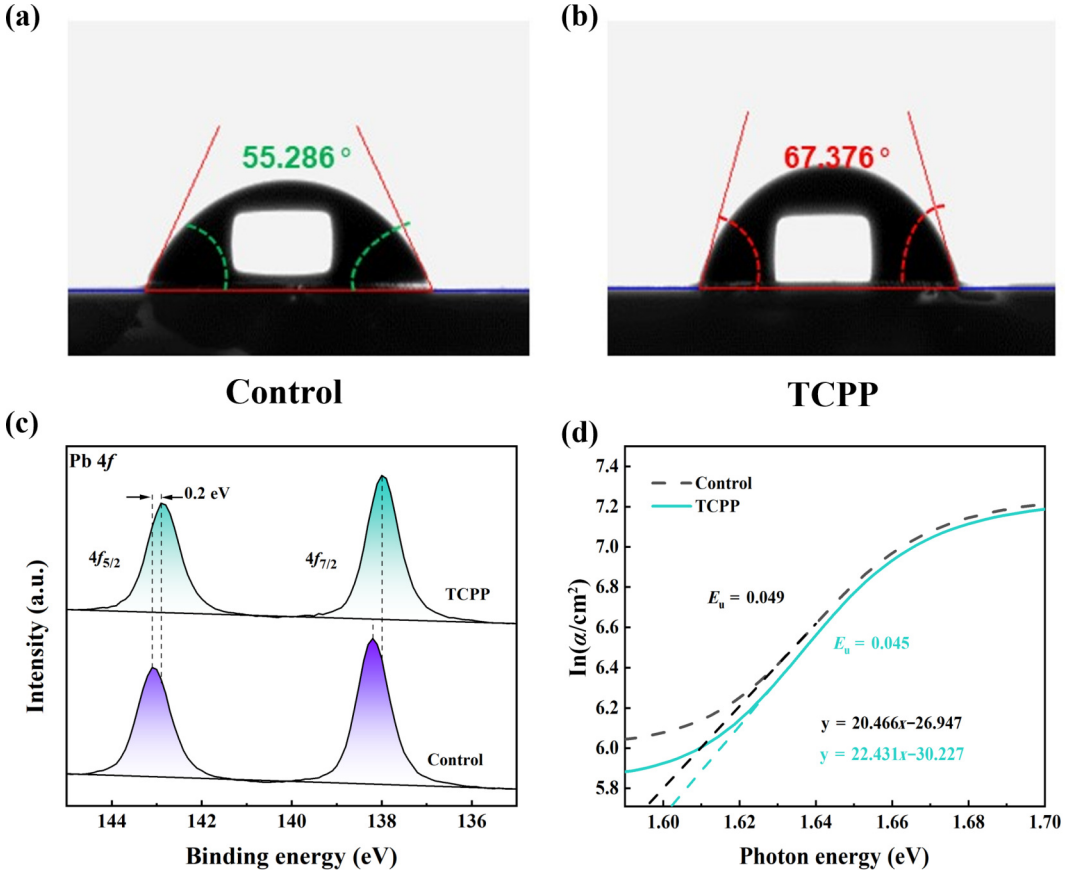

Figure 5 Characteristics of the control and modified perovskite films. (a) and (b) Contact angles. (c) XPS spectra of Pb 4*f* orbital. (d) Calculation of Urbach energy from the absorption tail.

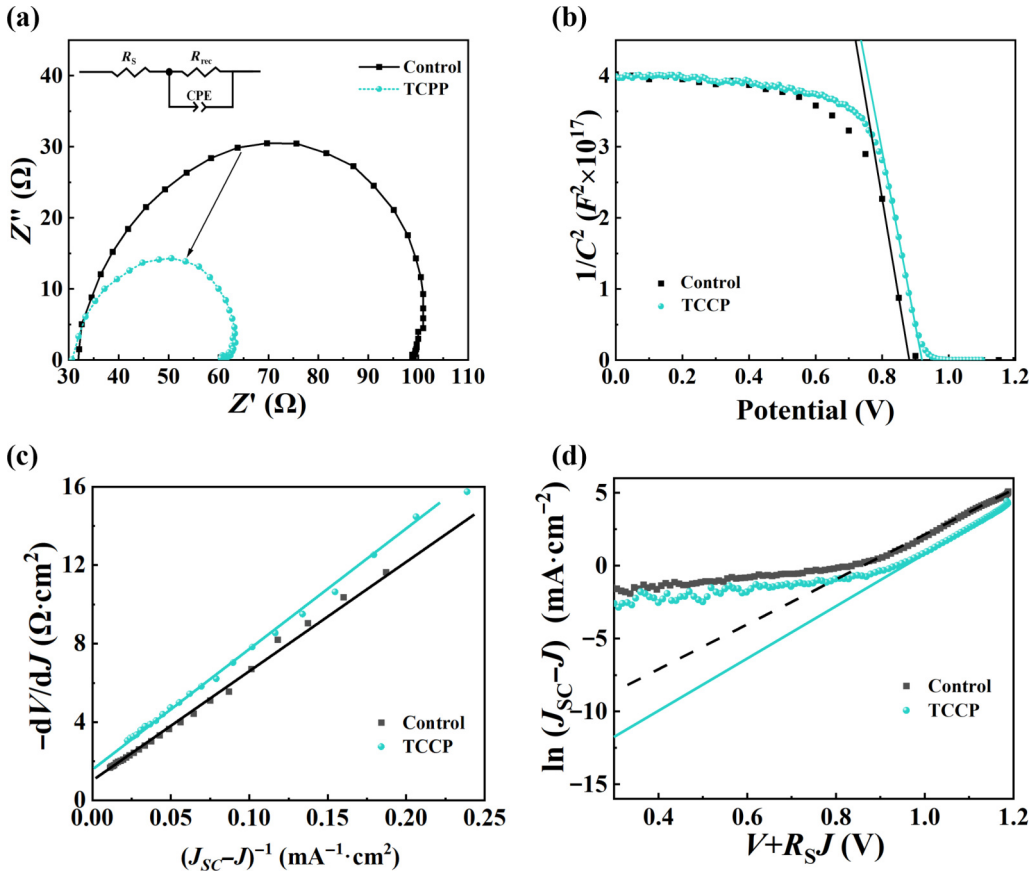

Figure 6 Characteristics of the control and modified PSCs. (a) Nyquist plots of the electrochemical impedance spectra. (b) Mott-Schottky plot of the capacitance-voltage characteristics. (c) and (d) Plots of dV/dJ versus $(J_{SC}-J)^{-1}$and ln $(J_{SC}-J)$ versus $(V+R_SJ)$ extracted from $J-V$ curves. The straight lines show the linear fittings.

ESM. The plots of $-dV/dJ$ versus $(J_{SC}-J)^{-1}$and $\ln(J_{SC}-J)$ versus $(V+JR_S)$ are shown in Figs. 6(c) and 6(d), respectively, and the extracted values can be found in Table S9 in the ESM. The PSCs with TCPP modification demonstrate a comparable series resistance (R_S) to that of the control device (2.94 and 2.87 Ω·cm^2, respectively), reflecting their similar J_{SC} values. The J_0 values for the control and TCPP-modified PSCs are 1.7×10^{-6} and 3.71×10^{-8} mA·cm^{-2}, respectively. Since J_0 is directly linked to the recombination rate [49], the decreased J_0 observed under TCPP modification indicates reduced recombination losses in the corresponding PSCs. According to the relation of $V_{OC}=(mK_BT/e)\ln((J_{SC}/J_0)+1)$, smaller J_0 leads to larger V_{OC}. Therefore, PSCs with TCPP interface modification exhibit a larger V_{OC} compared to those without interface modification. The dark J-V characteristics depicted in Fig. S5 in the ESM also indicate a smaller J_0 and reduced recombination loss in the TCPP-modified device.

3 Conclusions

This study demonstrates that the introduction of TCPP significantly improves the overall performance and stability of perovskite solar cells. The enhanced crystallization, coupled with effective passivation of both deep and shallow defects, contributes to reduced nonradiative recombination and a notable increase in carrier lifetimes. The device structure incorporating TCPP-modified perovskite layers achieved a peak PCE of 20.73%, a substantial improvement over the control devices. Additionally, the TCPP modification reduces defect-assisted recombination and enhances the built-in potential, as evidenced by electrochemical impedance and Mott-Schottky analyses. These changes are further supported by improved photoluminescence intensity and extended carrier lifetimes observed in TRPL measurements. Furthermore, the TCPP-modified perovskite films demonstrated superior environmental stability, including enhanced resistance to moisture ingress, as indicated by the increased contact angle and stable surface morphology. The findings underscore the potential of cost-effective and multifunctional molecules like TCPP for advancing perovskite solar cell technology. This approach not only addresses key challenges associated with efficiency and stability but also provides a scalable solution for commercial deployment. Future studies could explore other organophosphorus ligands or similar multifunctional molecules to further optimize the device performance and adapt this methodology to different perovskite compositions or architectures.

Acknowledgements

We gratefully acknowledge support from the National Natural Science Foundation of China under (Nos. 62075006 and 52075289).

Declaration of conflicting interests

The authors declare no conflicting interests regarding the content of this article.

Data availability

All data needed to support the conclusions in the paper are presented in the manuscript and/or the Supplementary Materials.

Additional data related to this paper may be requested from the corresponding author upon request.

Electronic Supplementary Material: Supplementary material (experimental details, characterization, theory calculation, and some other information of devices and films) is available in the online version of this article at https://doi.org/10.26599/NRE.2025.9120157.

References

[1] Park, N. G. Perovskite solar cells: An emerging photovoltaic technology. *Mater. Today* **2015**, *18*, 65–72.

[2] Unger, E. L.; Kegelmann, L.; Suchan, K.; Sörell, D.; Korte, L.; Albrecht, S. Roadmap and roadblocks for the band gap tunability of metal halide perovskites. *J. Mater. Chem. A* **2017**, *5*, 11401–11409.

[3] Xiao, X.; Wu, M.; Ni, Z. Y.; Xu, S.; Chen, S. S.; Hu, J.; Rudd, P. N.; You, W.; Huang, J. S. Ultrafast exciton transport with a long diffusion length in layered perovskites with organic cation functionalization. *Adv. Mater.* **2020**, *32*, 2004080.

[4] Turren-Cruz, S. H.; Saliba, M.; Mayer, M. T.; Juárez-Santiesteban, H.; Mathew, X.; Nienhaus, L.; Tress, W.; Erodici, M. P.; Sher, M. J.; Bawendi, M. G. et al. Enhanced charge carrier mobility and lifetime suppress hysteresis and improve efficiency in planar perovskite solar cells. *Energy Environ. Sci.* **2018**, *11*, 78–86.

[5] Yang, Y.; Yang, M. J.; Li, Z.; Crisp, R.; Zhu, K.; Beard, M. C. Comparison of recombination dynamics in $CH_3NH_3PbBr_3$ and $CH_3NH_3PbI_3$ perovskite films: Influence of exciton binding energy. *J. Phys. Chem. Lett.* **2015**, *6*, 4688–4692.

[6] Lin, H.; Yang, M.; Ru, X. N.; Wang, G. S.; Yin, S.; Peng, F. G.; Hong, C. J.; Qu, M. H.; Lu, J. X.; Fang, L. et al. Silicon heterojunction solar cells with up to 26.81% efficiency achieved by electrically optimized nanocrystalline-silicon hole contact layers. *Nat. Energy* **2023**, *8*, 789–799.

[7] Wu, J. H.; Shi, J. J.; Li, Y. M.; Li, H. S.; Wu, H. J.; Luo, Y. H.; Li, D. M.; Meng, Q. B. Quantifying the interface defect for the stability origin of perovskite solar cells. *Adv. Energy Mater.* **2019**, *9*, 1901352.

[8] Chen, R.; Wang, J. N.; Liu, Z. H.; Ren, F. M.; Liu, S. W.; Zhou, J.; Wang, H. X.; Meng, X.; Zhang, Z.; Guan, X. Y. et al. Reduction of bulk and surface defects in inverted methylammonium- and bromide-free formamidinium perovskite solar cells. *Nat. Energy* **2023**, *8*, 839–849.

[9] Chen, J. Z.; Park, N. G. Causes and solutions of recombination in perovskite solar cells. *Adv. Mater.* **2019**, *31*, 1803019.

[10] Song, D. D.; Ji, J.; Li, Y. Y.; Li, G. Y.; Li, M. C.; Wang, T. Y.; Wei, D.; Cui, P.; He, Y.; Mbengue, J. M. Degradation of organometallic perovskite solar cells induced by trap states. *Appl. Phys. Lett.* **2016**, *108*, 093901.

[11] Cai, Q. R.; Yao, Y.; Lu, Y.; Wang, M. L.; Zhang, Y. Q.; Song, D. D.; Xu, Z.; Li, X. D.; Wei, D. Stable perovskite solar cells with 22% efficiency enabled by inhibiting migration/loss of iodide ions. *Phys. Chem. Chem. Phys.* **2023**, *25*, 6955–6962.

[12] Wu, Z. F.; Bi, E. B.; Ono, L. K.; Li, D. B.; Bakr, O. M.; Yan, Y. F.; Qi, Y. B. Passivation strategies for enhancing device performance of perovskite solar cells. *Nano Energy* **2023**, *115*, 108731.

[13] Enkhbayar, E.; Otgontamir, N.; Kim, S.; Lee, J.; Kim, J. Understanding of defect passivation effect on wide band gap p–i–n perovskite solar cell. *ACS Appl. Mater. Interfaces* **2024**, *16*, 35084–35094.

[14] Liao, Q. H.; Zhu, K. X.; Hao, X. Z.; Wu, C. X.; Li, J.; Cheng, H. H.; Yan, J. F.; Jiang, L.; Qu, L. T. Bio-inspired ultrathin perfect absorber for high-performance photothermal conversion. *Adv. Mater.* **2024**, *36*, 2313366.

[15] Guo, H.; Xie, J. W.; He, G. Z.; Zhu, D. Z.; Qiao, M.; Yan, J. F.; Yu, J. C.; Li, J. Q.; Zhao, Y. Z.; Luo, M. et al. A review of ultrafast laser micro/nano fabrication: Material processing, surface/interface controlling, and devices fabrication. *Nano Res.* **2024**, *17*, 6212–6230.

[16] Wang, Y.; Li, L. C.; Wu, Z. J.; Zhang, R. K.; Hong, J.; Zhang, J. X.; Rao, H. S.; Pan, Z. X.; Zhong, X. H. Self-driven prenucleation-induced perovskite crystallization enables efficient perovskite solar cells. *Angew. Chem., Int. Ed.* **2023**, *62*, e202302342.

[17] Wu, N.; Yang, T. H.; Wang, Z. C.; Wu, Y.; Wang, Y. J.; Ma, C.; Li, H. J.; Du, Y. C.; Zhao, D.; Wang, S. et al. Stabilizing precursor solution and controlling crystallization kinetics simultaneously for high-performance perovskite solar cells. *Adv. Mater.* **2023**, *35*, 2304809.

[18] Wu, T.; Wang, P.; Zheng, L. D.; Zhao, Y. J.; Hua, Y. Perovskite crystallization and hot carrier dynamics manipulation enables efficient and stable perovskite solar cells with 25.32% efficiency. *Adv. Energy Mater.* **2024**, *14*, 2400078.

[19] Xiong, S. B.; Tian, F. Y.; Wang, F.; Cao, A. P.; Chen, Z.; Jiang, S.; Li, D.; Xu, B.; Wu, H. B.; Zhang, Y. F. et al. Reducing nonradiative recombination for highly efficient inverted perovskite solar cells via a synergistic bimolecular interface. *Nat. Commun.* **2024**, *15*, 5607.

[20] Liu, B. B.; Ren, X. D.; Li, R.; Chen, Y.; He, D. M.; Li, Y.; Zhou, Q.; Ma, D. Q.; Han, X.; Shai, X. et al. Stabilizing top interface by molecular locking strategy with polydentate chelating biomaterials toward efficient and stable perovskite solar cells in ambient air. *Adv. Mater.* **2024**, *36*, 2312679.

[21] Yang, B. W.; Suo, J. J.; Bogachuk, D.; Kaiser, W.; Baretzky, C.; Er-Raji, O.; Loukeris, G.; Alothman, A. A.; Mosconi, E.; Kohlstädt, M. et al. A universal ligand for lead coordination and tailored crystal growth in perovskite solar cells. *Energy Environ. Sci.* **2024**, *17*, 1549–1558.

[22] Warby, J.; Shah, S.; Thiesbrummel, J.; Gutierrez-Partida, E.; Lai, H. G.; Alebachew, B.; Grischek, M.; Yang, F. J.; Lang, F.; Albrecht, S. et al. Mismatch of quasi-fermi level splitting and V_{OC} in perovskite solar cells. *Adv. Energy Mater.* **2023**, *13*, 2303135.

[23] Wang, S. L.; Sun, H. R.; Wang, P. Y.; Ge, X.; Li, Y. C.; Li, D. N.; Huang, Q.; Du, X. N.; Zhao, Y.; Zhang, X. D. Small molecule regulatory strategy for inorganic perovskite solar cells with 368 mV of V_{OC} deficit and its application in tandem devices. *Adv. Energy Mater.* **2024**, *14*, 2400151.

[24] Huo, X. M.; Mariotti, S.; Li, Y. Y.; Ding, C. F.; Ji, P. H.; Yuan, S.; Li, T. T.; Meng, N.; Liu, X. M.; Zhang, J. H. et al. Unraveling the relationship between the phenethylammonium-induced 2D phase on the perovskite surface and inverted wide bandgap perovskite solar cell performance. *Energy Environ. Sci.* **2024**, *17*, 8658–8669.

[25] Huo, X. M.; Li, Y. Y.; Liu, W.; Huang, X. F.; Meng, J.; Lu, Y.; Meng, N.; Zhang, Y.; Zhao, S. L.; Qiao, B. et al. Nonpolar and ultra-long-chain ligand to modify the perovskite interface toward high-efficiency and stable wide bandgap perovskite solar cells. *ACS Appl. Energy Mater.* **2023**, *6*, 1731–1740.

[26] Shi, L.; Bucknall, M. P.; Young, T. L.; Zhang, M.; Hu, L.; Bing, J. M.; Lee, D. S.; Kim, J.; Wu, T.; Takamure, N. et al. Gas chromatography-mass spectrometry analyses of encapsulated stable perovskite solar cells. *Science* **2020**, *368*, eaba2412.

[27] Landi, G.; Neitzert, H. C.; Barone, C.; Mauro, C.; Lang, F.; Albrecht, S.; Rech, B.; Pagano, S. Correlation between electronic defect states distribution and device performance of perovskite solar cells. *Adv. Sci.* **2017**, *4*, 1700183.

[28] Azmi, R.; Nurrosyid, N.; Lee, S. H.; Al Mubarok, M.; Lee, W.; Hwang, S.; Yin, W. P.; Ahn, T. K.; Kim, T. W.; Ryu, D. Y. et al. Shallow and deep trap state passivation for low-temperature processed perovskite solar cells. *ACS Energy Lett.* **2020**, *5*, 1396–1403.

[29] Antonopoulou, M.; Giannakas, A.; Bairamis, F.; Papadaki, M.; Konstantinou, I. Degradation of organophosphorus flame retardant tris (1-chloro-2-propyl) phosphate (TCPP) by visible light N, S-codoped TiO_2 photocatalysts. *Chem. Eng. J.* **2017**, *318*, 231–239.

[30] Xu, X.; Cai, Y. T.; Qu, Y. T.; Li, A.; Gao, Y. J.; Huang, T. C.; Wu, Z. X.; Huang, X.; Zhang, Z. Y.; Wu, Z. Y. et al. Defect evolution of iodine vacancy and related strain modulation in all-inorganic halide perovskites. *Appl. Phys. Lett.* **2023**, *123*, 122105.
[31] Feng, X. X.; Li, Y. H.; Liu, B.; Tong, C. J.; Long, M. Q.; Cai, M. Q.; Yang, J. L. Iodide vacancy defects clustering in pairs rather than in isolation in a lead iodide perovskite: Identification, origin, and implications. *J. Phys. Chem. Lett.* **2024**, *15*, 2209–2215.
[32] Ray, A.; Martín-García, B.; Prato, M.; Moliterni, A.; Bordignon, S.; Spirito, D.; Marras, S.; Goldoni, L.; Boopathi, K. M.; Moro, F. et al. Mixed organic cations promote ambient light-induced formation of metallic lead in lead halide perovskite crystals. *ACS Appl. Mater. Interfaces* **2023**, *15*, 28166–28174.
[33] Hossain, M. K.; Mohammed, M. K. A.; Pandey, R.; Arnab, A. A.; Rubel, M. H. K.; Hossain, K. M.; Ali, H.; Rahman, F.; Bencherif, H.; Madan, J. et al. Numerical analysis in DFT and SCAPS-1D on the influence of different charge transport layers of $CsPbBr_3$ perovskite solar cells. *Energy Fuels* **2023**, *37*, 6078–6098.
[34] Meng, N.; Huang, X. F.; Huo, X. M.; Liang, Z. Q.; Wei, D.; Zhao, S. L.; Qiao, B.; Liang, Z. Q.; Xu, Z.; Song, D. D. Increasing the wettability and reducing excess PbI_2 using diamine hydrobromides with different lengths at the buried interface of the 3D perovskite film. *J. Mater. Chem. C* **2023**, *11*, 15959–15966.
[35] Ryu, S.; Gil, B.; Kim, B.; Kim, J.; Park, B. Understanding the trap characteristics of perovskite solar cells via drive-level capacitance profiling. *ACS Appl. Mater. Interfaces* **2023**, *15*, 56909–56917.
[36] Chen, J.; Lou, Y. H.; Wang, Z. K. Characterizing spatial and energetic distributions of trap states toward highly efficient perovskite photovoltaics. *Small* **2023**, *19*, 2305064.
[37] Yousuf, R.; Qazi, G. Numerical modelling and impact analysis of traps incurred performance deterioration of perovskite solar cells using η_{qe} curves, SRH and solar cell model. *Opt. Quant. Electron.* **2023**, *55*, 227.
[38] Jubu, P. R.; Obaseki, O. S.; Ajayi, D. I.; Danladi, E.; Chahrour, K. M.; Muhammad, A.; Landi, S. Jr.; Igbawua, T.; Chahul, H. F.; Yam, F. K. Considerations about the determination of optical bandgap from diffuse reflectance spectroscopy using the Tauc plot. *J. Opt.* **2024**, *53*, 5054–5064.
[39] Si, H. N.; Zhang, S. C.; Ma, S. F.; Xiong, Z. Z.; Kausar, A.; Liao, Q. L.; Zhang, Z.; Sattar, A.; Kang, Z.; Zhang, Y. Emerging conductive atomic force microscopy for metal halide perovskite materials and solar cells. *Adv. Energy Mater.* **2020**, *10*, 1903922.
[40] Wang, X. X.; Huang, H.; Wang, M.; Lan, Z. N.; Cui, P.; Du, S. X.; Yang, Y. Y.; Yan, L. Y.; Zhang, Q.; Qu, S. J. et al. Oriented molecular bridge constructs homogeneous buried interface for perovskite solar cells with efficiency over 25.3%. *Adv. Mater.* **2024**, *36*, 2310710.
[41] Li, C.; Zhang, N.; Gao, P. Lessons learned: How to report XPS data incorrectly about lead-halide perovskites. *Mater. Chem. Front.* **2023**, *7*, 3797–3802.
[42] Artuk, K.; Turkay, D.; Mensi, M. D.; Steele, J. A.; Jacobs, D. A.; Othman, M.; Yu Chin, X.; Moon, S. J.; Tiwari, A. N.; Hessler-Wyser, A. et al. A universal perovskite/C_{60} interface modification via atomic layer deposited aluminum oxide for perovskite solar cells and perovskite-silicon tandems. *Adv. Mater.* **2024**, *36*, 2311745.
[43] Tian, S. T.; Huang, T. Y.; Han, F.; Wang, F. Z.; Tan, Z.; Bai, Y. M. Optimization of tail state Urbach energy enables efficient organic solar cells and perovskite/organic tandem solar cells. *Org. Electron.* **2023**, *113*, 106714.
[44] Hu, X. D.; Pan, Y. Y.; Wang, J. N.; Liu, Z. H.; Chen, W. Reducing energy disorder by stabilizing octahedral lattice with thiocyanate for efficient and stable Sn–Pb mixed perovskite solar cells. *Nano Energy* **2023**, *118*, 108937.
[45] Schultz, C.; Fenske, M.; Dion-Bertrand, L. I.; Gélinas, G.; Marcet, S.; Dagar, J.; Bartelt, A.; Schlatmann, R.; Unger, E.; Stegemann, B. Hyperspectral photoluminescence imaging for spatially resolved determination of electrical parameters of laser-patterned perovskite solar cells. *Sol. RRL* **2023**, *7*, 2300538.
[46] Mei, B. A.; Munteshari, O.; Lau, J.; Dunn, B.; Pilon, L. Physical interpretations of Nyquist plots for EDLC electrodes and devices. *J. Phys. Chem. C* **2018**, *122*, 194–206.
[47] Feng, Y. L.; Bian, J. M.; Wang, S.; Zhang, C. Y.; Wang, M. H.; Shi, Y. T. Soft interfaces within hybrid perovskite solar cells: Real-time dynamic tracking of interfacial electrical property evolution by EIS. *J. Mater. Chem. C* **2019**, *7*, 8294–8302.
[48] Zhang, J. S.; Li, J. B.; Duan, J. L.; Zhang, X. Y.; Dou, J.; Guo, Q. Y.; Jiang, C.; Zhao, Y. Y.; Huang, H.; Tang, Q. W. Ionic-rich vermiculite tailoring dynamic bottom-up gradient for high-efficiency perovskite solar cells. *Adv. Funct. Mater.* **2024**, *34*, 2401662.
[49] Saliba, M.; Etgar, L. Current density mismatch in perovskite solar cells. *ACS Energy Lett.* **2020**, *5*, 2886–2888.

Yaoyao Li is a postdoctoral in the Department of Mechanical Engineering at Tsinghua University. He received his Ph.D degree in Optical Engineering from Beijing Jiaotong University in 2024. His current research interest focuses on micro/nano functional devices and nano materials.

Jianfeng Yan is an Associate Professor at Tsinghua University. He received his Ph.D degree of Engineering from Tsinghua University in 2013. His current research interests are in the fields of micro/nano fabrication, ultrafast laser processing and micro/nano functional devices.

Dandan Song is a Professor at Beijing Jiaotong University. She received her Ph.D degree in Optics from Beijing Jiaotong University in 2011. Her research interests lie in the applications of machine learning in light-emitting devices, solar cells, and nano materials.